



# Wavelength-selective mid-infrared metamaterial absorbers with multiple tungsten cross resonators

ZHIGANG LI,<sup>1</sup> LILIANA STAN,<sup>2</sup> DAVID A. CZAPLEWSKI,<sup>2</sup> XIAODONG YANG,<sup>1</sup> AND JIE GAO<sup>1,\*</sup>

<sup>1</sup>Department of Mechanical and Aerospace Engineering, Missouri University of Science and Technology, Rolla, MO 65409, USA

<sup>2</sup>Center for Nanoscale Materials, Argonne National Laboratory, Argonne, IL 60439, USA

\*gaojie@mst.edu

**Abstract:** Wavelength-selective metamaterial absorbers in the mid-infrared range are demonstrated by using multiple tungsten cross resonators. By adjusting the geometrical parameters of cross resonators in single-sized unit cells, near-perfect absorption with single absorption peak tunable from 3.5  $\mu\text{m}$  to 5.5  $\mu\text{m}$  is realized. The combination of two, three, or four cross resonators of different sizes in one unit cell enables broadband near-perfect absorption at mid-infrared range. The obtained absorption spectra exhibit omnidirectionality and weak dependence on incident polarization. The underlying mechanism of near-perfect absorption with cross resonators is further explained by the optical mode analysis, dispersion relation and equivalent RLC circuit model. Moreover, thermal analysis is performed to study the heat generation and temperature increase in the cross resonator absorbers, while the energy conversion efficiency is calculated for the thermophotovoltaic system made of the cross resonator thermal emitters and low-bandgap semiconductors.

© 2018 Optical Society of America under the terms of the [OSA Open Access Publishing Agreement](#)

**OCIS codes:** (300.1030) Absorption; (260.5740) Resonance; (130.3060) Infrared.

## References and links

1. S. B. Glybovski, S. A. Tretyakov, P. A. Belov, Y. S. Kivshar, and C. R. Simovski, "Metasurfaces: From microwaves to visible," *Phys. Rep.* **634**, 1–72 (2016).
2. N. I. Landy, S. Sajuyigbe, J. J. Mock, D. R. Smith, and W. J. Padilla, "Perfect metamaterial absorber," *Phys. Rev. Lett.* **100**(20), 207402 (2008).
3. Y. Cui, Y. He, Y. Jin, F. Ding, L. Yang, Y. Ye, S. Zhong, Y. Lin, and S. He, "Plasmonic and metamaterial structures as electromagnetic absorbers," *Laser Photonics Rev.* **8**(4), 495–520 (2014).
4. H. Deng, Z. Li, L. Stan, D. Rosenmann, D. Czaplewski, J. Gao, and X. Yang, "Broadband perfect absorber based on one ultrathin layer of refractory metal," *Opt. Lett.* **40**(11), 2592–2595 (2015).
5. C. M. Watts, D. Shrekenhamer, J. Montoya, G. Lipworth, J. Hunt, T. Sleasman, S. Krishna, D. R. Smith, and W. J. Padilla, "Terahertz compressive imaging with metamaterial spatial light modulators," *Nat. Photonics* **8**(8), 605–609 (2014).
6. H. T. Miyazaki, T. Kasaya, M. Iwanaga, B. Choi, Y. Sugimoto, and K. Sakoda, "Dual-band infrared metasurface thermal emitter for CO<sub>2</sub>sensing," *Appl. Phys. Lett.* **105**(12), 121107 (2014).
7. A. Lochbaum, Y. Fedoryshyn, A. Dorodnyy, U. Koch, C. Hafner, and J. Leuthold, "On-Chip Narrowband Thermal Emitter for Mid-IR Optical Gas Sensing," *ACS Photonics* **4**(6), 1371–1380 (2017).
8. E. Rephaeli and S. Fan, "Absorber and emitter for solar thermo-photovoltaic systems to achieve efficiency exceeding the Shockley-Queisser limit," *Opt. Express* **17**(17), 15145–15159 (2009).
9. H. A. Atwater and A. Polman, "Plasmonics for improved photovoltaic devices," *Nat. Mater.* **9**(3), 205–213 (2010).
10. C. Wu, B. Neuner III, J. John, A. Milder, B. Zollars, S. Savoy, and G. Shvets, "Metamaterial-based integrated plasmonic absorber/emitter for solar thermo-photovoltaic systems," *J. Opt.* **14**(2), 24005 (2012).
11. S. Molesky, C. J. Dewalt, and Z. Jacob, "High temperature epsilon-near-zero and epsilon-near-pole metamaterial emitters for thermophotovoltaics," *Opt. Express* **21**(S1), A96–A110 (2013).
12. J.-J. Greffet and M. Nieto-Vesperinas, "Field theory for generalized bidirectional reflectivity: derivation of Helmholtz's reciprocity principle and Kirchhoff's law," *J. Opt. Soc. Am. A* **15**(10), 2735–2744 (1998).
13. H. Deng, T. Wang, J. Gao, X. Yang, D. Huixu, W. Tianchen, G. Jie, and Y. Xiaodong, "Metamaterial thermal emitters based on nanowire cavities for high-efficiency thermophotovoltaics," *J. Opt.* **16**(3), 35102 (2014).
14. H. Wang, V. Prasad Sivan, A. Mitchell, G. Rosengarten, P. Phelan, and L. Wang, "Highly efficient selective

- metamaterial absorber for high-temperature solar thermal energy harvesting,” *Sol. Energy Mater. Sol. Cells* **137**, 235–242 (2015).
15. D. Woolf, J. Hensley, J. G. Cederberg, D. T. Bethke, A. D. Grine, and E. A. Shaner, “Heterogeneous metasurface for high temperature selective emission,” *Appl. Phys. Lett.* **105**(8), 081110 (2014).
  16. D. Costantini, A. Lefebvre, A.-L. Coutrot, I. Moldovan-Doyen, J.-P. Hugonin, S. Boutami, F. Marquier, H. Benisty, and J.-J. Greffet, “Plasmonic Metasurface for Directional and Frequency-Selective Thermal Emission,” *Phys. Rev. Appl.* **4**(1), 14023 (2015).
  17. H. Wang, Q. Chen, L. Wen, S. Song, X. Hu, and G. Xu, “Titanium-nitride-based integrated plasmonic absorber/emitter for solar thermophotovoltaic application,” *Photon. Res.* **3**(6), 329–334 (2015).
  18. C. M. Watts, X. Liu, and W. J. Padilla, “Metamaterial electromagnetic wave absorbers,” *Adv. Mater.* **24**, OP98 (2012).
  19. T. Inoue, M. De Zoysa, T. Asano, and S. Noda, “Realization of narrowband thermal emission with optical nanostructures,” *Optica* **2**(1), 27–35 (2015).
  20. K. Ikeda, H. T. Miyazaki, T. Kasaya, K. Yamamoto, Y. Inoue, K. Fujimura, T. Kanakugi, M. Okada, K. Hatade, and S. Kitagawa, “Controlled thermal emission of polarized infrared waves from arrayed plasmon nanocavities,” *Appl. Phys. Lett.* **92**(2), 2006–2009 (2008).
  21. Y. X. Yeng, M. Ghebrebrhan, P. Bermel, W. R. Chan, J. D. Joannopoulos, M. Soljačić, and I. Celanovic, “Enabling high-temperature nanophotonics for energy applications,” *Proc. Natl. Acad. Sci. U.S.A.* **109**(7), 2280–2285 (2012).
  22. J. G. Fleming, S. Y. Lin, I. El-Kady, R. Biswas, and K. M. Ho, “All-metallic three-dimensional photonic crystals with a large infrared bandgap,” *Nature* **417**(6884), 52–55 (2002).
  23. L. P. Wang and Z. M. Zhang, “Phonon-mediated magnetic polaritons in the infrared region,” *Opt. Express* **19**(S2), A126–A135 (2011).
  24. T. Inoue, M. De Zoysa, T. Asano, and S. Noda, “Single-peak narrow-bandwidth mid-infrared thermal emitters based on quantum wells and photonic crystals,” *Appl. Phys. Lett.* **102**(19), 10–14 (2013).
  25. H. Wang and L. Wang, “Perfect selective metamaterial solar absorbers,” *Opt. Express* **21**(S6), A1078–A1093 (2013).
  26. X. Liu, T. Tyler, T. Starr, A. F. Starr, N. M. Jokerst, and W. J. Padilla, “Taming the blackbody with infrared metamaterials as selective thermal emitters,” *Phys. Rev. Lett.* **107**(4), 045901 (2011).
  27. Y. Cui, J. Xu, K. Hung Fung, Y. Jin, A. Kumar, S. He, and N. X. Fang, “A thin film broadband absorber based on multi-sized nanoantennas,” *Appl. Phys. Lett.* **99**(25), 253101 (2011).
  28. A. Lefebvre, D. Costantini, I. Doyen, Q. Lévesque, E. Lorent, D. Jacolin, J.-J. Greffet, S. Boutami, and H. Benisty, “CMOS compatible metal-insulator-metal plasmonic perfect absorbers,” *Opt. Mater. Express* **6**(7), 2389 (2016).
  29. Y. Guo and Z. Jacob, “Thermal hyperbolic metamaterials,” *Opt. Express* **21**(12), 15014–15019 (2013).
  30. N. H. Shen, T. Koschny, M. Kafesaki, and C. M. Soukoulis, “Optical metamaterials with different metals,” *Phys. Rev. B* **85**, 075120 (2012).
  31. C.-W. Cheng, M. N. Abbas, C.-W. Chiu, K.-T. Lai, M.-H. Shih, and Y.-C. Chang, “Wide-angle polarization independent infrared broadband absorbers based on metallic multi-sized disk arrays,” *Opt. Express* **20**(9), 10376–10381 (2012).
  32. A. K. Azad, W. J. M. Kort-Kamp, M. Sykora, N. R. Weisse-Bernstein, T. S. Luk, A. J. Taylor, D. A. R. Dalvit, and H. T. Chen, “Metasurface Broadband Solar Absorber,” *Sci. Rep.* **6**(1), 20347 (2016).
  33. H. Deng, L. Stan, D. A. Czaplewski, J. Gao, and X. Yang, “Broadband infrared absorbers with stacked double chromium ring resonators,” *Opt. Express* **25**(23), 28295–28304 (2017).
  34. S. He, F. Ding, L. Mo, and F. Bao, “Light Absorber with an Ultra-Broad Flat Band Based on Multi-Sized Slow-Wave Hyperbolic Metamaterial Thin-Films,” *Prog. Electromagnetics Res.* **147**, 69–79 (2014).
  35. D. Ji, H. Song, X. Zeng, H. Hu, K. Liu, N. Zhang, and Q. Gan, “Broadband absorption engineering of hyperbolic metafilm patterns,” *Sci. Rep.* **4**(1), 4498 (2014).
  36. J. A. Bossard, L. Lin, S. Yun, L. Liu, D. H. Werner, and T. S. Mayer, “Near-ideal optical metamaterial absorbers with super-octave bandwidth,” *ACS Nano* **8**(2), 1517–1524 (2014).
  37. S. Han, J.-H. Shin, P.-H. Jung, H. Lee, and B. J. Lee, “Broadband Solar Thermal Absorber Based on Optical Metamaterials for High-Temperature Applications,” *Adv. Opt. Mater.* **4**(8), 1265–1273 (2016).
  38. J. Zeng, L. Li, X. Yang, and J. Gao, “Generating and Separating Twisted Light by gradient-rotation Split-Ring Antenna Metasurfaces,” *Nano Lett.* **16**(5), 3101–3108 (2016).
  39. L. Sun, Z. Li, T. S. Luk, X. Yang, and J. Gao, “Nonlocal effective medium analysis in symmetric metal-dielectric multilayer metamaterials,” *Phys. Rev. B* **91**(19), 195147 (2015).
  40. Z. Li, W. Wang, D. Rosenmann, D. A. Czaplewski, X. Yang, and J. Gao, “All-metal structural color printing based on aluminum plasmonic metasurfaces,” *Opt. Express* **24**(18), 20472–20480 (2016).
  41. W. Wang, D. Rosenmann, D. A. Czaplewski, X. Yang, and J. Gao, “Realizing structural color generation with aluminum plasmonic V-groove metasurfaces,” *Opt. Express* **25**(17), 20454–20465 (2017).
  42. A. D. Rakic, A. B. Djurisic, J. M. Elazar, and M. L. Majewski, “Optical properties of metallic films for vertical-cavity optoelectronic devices,” *Appl. Opt.* **37**(22), 5271–5283 (1998).
  43. J. Kischkat, S. Peters, B. Gruska, M. Semtsiv, M. Chashnikova, M. Klinkmüller, O. Fedosenko, S. Machulik, A. Aleksandrova, G. Monastyrskyi, Y. Flores, and W. T. Masselink, “Mid-infrared optical properties of thin films of aluminum oxide, titanium dioxide, silicon dioxide, aluminum nitride, and silicon nitride,” *Appl. Opt.* **51**(28),

- 6789–6798 (2012).
44. J. B. Pendry, L. Martín-Moreno, and F. J. Garcia-Vidal, “Mimicking surface plasmons with structured surfaces,” *Science* **305**(5685), 847–848 (2004).
  45. B. Zhao, L. Wang, Y. Shuai, and Z. M. Zhang, “Thermophotovoltaic emitters based on a two-dimensional grating/thin-film nanostructure,” *Int. J. Heat Mass Transf.* **67**, 637–645 (2013).
  46. A. Barbara, S. Collin, C. Sauvan, J. Le Perchec, C. Maxime, J.-L. Pelouard, and P. Quémerais, “Plasmon dispersion diagram and localization effects in a three-cavity commensurate grating,” *Opt. Express* **18**(14), 14913–14925 (2010).
  47. Y. B. Chen and C. J. Chen, “Interaction between the magnetic polariton and surface plasmon polariton,” *Opt. Commun.* **297**, 169–175 (2013).
  48. F. Costa, S. Genovesi, A. Monorchio, and G. Manara, “A circuit-based model for the interpretation of perfect metamaterial absorbers,” *IEEE Trans. Antenn. Propag.* **61**(3), 1201–1209 (2013).
  49. A. Sakurai, B. Zhao, and Z. M. Zhang, “Resonant frequency and bandwidth of metamaterial emitters and absorbers predicted by an RLC circuit model,” *J. Quant. Spectrosc. Radiat. Transf.* **149**, 33–40 (2014).
  50. Z. M. Zhang, *Nano/Microscale Heat Transfer* (McGraw-Hill, 2007).
  51. H. Haus, *Waves and Fields in Optoelectronics* (Prentice-Hall, 1985).
  52. G. Baffou, R. Quidant, and F. J. García De Abajo, “Nanoscale control of optical heating in complex plasmonic systems,” in *ACS Nano* (ACS, 2010), Vol. 4, pp. 709–716.
  53. X. Chen, Y. Chen, M. Yan, and M. Qiu, “Nanosecond photothermal effects in plasmonic nanostructures,” *ACS Nano* **6**(3), 2550–2557 (2012).
  54. I. Stark, M. Stordeur, and F. Syrowatka, “Thermal conductivity of thin amorphous alumina films,” *Thin Solid Films* **226**(1), 185–190 (1993).
  55. R. M. Costescu, D. G. Cahill, F. H. Fabreguette, Z. A. Sechrist, and S. M. George, “Ultra-Low Thermal Conductivity in W/Al<sub>2</sub>O<sub>3</sub> Nanolaminates,” *Science* **303**(5660), 989–990 (2004).
  56. J. Martan, N. Semmar, C. Boulmer-Leborgne, P. Plantin, and E. Le Menn, “Thermal Characterization of Tungsten Thin Films by Pulsed Photothermal Radiometry,” *Nanoscale Microscale Thermophys. Eng.* **10**(4), 333–344 (2006).
  57. C. Ferrari, F. Melino, M. Pinelli, P. R. Spina, and M. Venturini, “Overview and status of thermophotovoltaic systems,” *Energy Procedia* **45**, 160–169 (2014).
  58. A. Krier, M. Yin, A. R. J. Marshall, and S. E. Krier, “Low Bandgap InAs-Based Thermophotovoltaic Cells for Heat-Electricity Conversion,” *J. Electron. Mater.* **45**(6), 2826–2830 (2016).
  59. C. Liu, Y. Li, and Y. Zeng, “Progress in Antimonide Based III-V Compound Semiconductors and Devices,” *Engineering* **2**(8), 617–624 (2010).
  60. M. V. Kovalenko, W. Heiss, E. V. Shevchenko, J. S. Lee, H. Schwinghammer, A. P. Alivisatos, and D. V. Talapin, “SnTe nanocrystals: A new example of narrow-gap semiconductor quantum dots,” *J. Am. Chem. Soc.* **129**(37), 11354–11355 (2007).
  61. S.-H. Wei and A. Zunger, “Electronic and structural anomalies in lead chalcogenides,” *Phys. Rev. B* **55**(20), 13605–13610 (1997).
  62. W. H. Strehlow and E. L. Cook, “Compilation of Energy Band Gaps in Elemental and Binary Compound Semiconductors and Insulators,” *J. Phys. Chem. Ref. Data* **2**(1), 163–200 (1973).
  63. J. Tang and E. H. Sargent, “Infrared colloidal quantum dots for photovoltaics: Fundamentals and recent progress,” *Adv. Mater.* **23**(1), 12–29 (2011).
  64. M. G. Mauk and V. M. Andreev, “GaSb-related materials for TPV cells,” *Semicond. Sci. Technol.* **18**(5), S191–S201 (2003).
  65. K. J. Cheetham, P. J. Carrington, N. B. Cook, and A. Krier, “Low bandgap GaInAsSbP pentanary thermophotovoltaic diodes,” *Sol. Energy Mater. Sol. Cells* **95**(2), 534–537 (2011).
  66. W. Shockley and H. J. Queisser, “Detailed balance limit of efficiency of p-n junction solar cells,” *J. Appl. Phys.* **32**(3), 510–519 (1961).

## 1. Introduction

Metamaterials exhibit intriguing electromagnetic properties with flexibly tailored permittivity and permeability through engineering the geometrical shape and material composition of artificial meta-atoms [1]. One important application of metamaterials is perfect light absorbers and thermal emitters used for promising applications of energy harvesting, imaging, sensor, and optical communication [2–4]. Metamaterial perfect absorbers in the mid-infrared range are appealing to various applications such as thermal imaging system with spatial light manipulation [5], molecular or gas sensing with low cost [6,7], and thermophotovoltaics (TPV) with conversion efficiency exceeding the Shockley-Queisser (SQ) limit [8–11]. Thermal emitters play key roles in TPV systems with heat energy directly converted into electric power. Since the emissivity of a material equals to the absorptivity at equilibrium according to the Kirchhoff’s law [12], the thermal emission spectrum of a metamaterial at a certain temperature can be equivalently predicted by its light absorption spectrum. For TPV

system with relatively high-bandgap semiconductor such as GaSb (0.71 eV), it requires a narrowband metamaterial thermal emitter with resonant wavelength shorter than 1.75  $\mu\text{m}$  and radiation suppression at other wavelengths for getting optimal conversion efficiency [13]. By considering the thermal stability, high temperature-enduring refractive metals (e.g. Ti [14], W [8], Pt [15,16]) and dielectrics (e.g.  $\text{Al}_2\text{O}_3$  [7], TiN [17]) are preferred materials for constructing the metamaterial thermal emitters.

In terms of the materials used, metamaterial absorbers can be mainly categorized into three types: all-metallic, metal-dielectric and all-dielectric metamaterial absorbers [18,19]. All-metallic micro-/nano-cavities or photonic crystal structures in 1D [20], 2D [21] and 3D [22] have been widely investigated for efficient light absorption, owing to the advantages of intrinsic thermal stability and enhanced photonic density of states. In contrast, all-dielectric structures are able to realize a narrow absorption window via surface phonon polaritons or inter-subband transitions [23,24]. Metal-dielectric metamaterials are known as perfect absorbers or emitters with the excitation of plasmonic magnetic resonance at certain wavelength [2,25–28]. The metal-insulator-metal (MIM) structures are usually designed as a combination of a metallic ground plane, a dielectric spacer and a top patterned metallic layer with resonators. Various geometries have been designed to obtain wavelength-selective metamaterial absorbers with omnidirectional and polarization-independent properties, including simple multilayer [29], ring resonator [2], fishnet [30], patch resonator [25], cross resonator [26] and other complex structures [1]. Since the resonance wavelength of a single resonator highly depends on its geometrical design, methods have been developed by combining dual or multiple resonators with different sizes in one unit cell in order to obtain the multi-band or broadband absorption, including multi-width strips [27], multiple patches [28], cross resonators [26], disks [31] and mixture of cross and disk resonators [32], as well as stacked double ring resonators [33]. The metal-dielectric multilayers are also used to realize ultra-broadband absorption with either 1D gratings [34] or 2D trapezoid cavities [35] based on the stop-light waveguide theory and structured metamaterial absorber through multiple overlapping resonances [36,37].

In this work, wavelength-selective metamaterial absorbers in the mid-infrared range are demonstrated by using single-sized and double-sized unit cells of tungsten cross resonators to obtain single peak, dual-band and broadband near-perfect absorption (or emission) at mid-infrared range. The design and optimization of metamaterial absorbers are discussed, followed by the experimental characterization of the absorption spectra. The underlying mechanism of near-perfect absorption in cross resonators is explained with the excitation of optical magnetic resonances for both TM and TE polarized incidence, and is further modelled by equivalent RLC circuit for intuitive understanding. Finally, potential applications at mid-infrared range for metamaterial absorbers and emitters are analyzed through the thermal analysis for heat generation and temperature increase, as well as the energy conversion efficiency calculation for low-temperature TPV system based on low-bandgap semiconductors.

## 2. Design and characterization of mid-infrared absorbers

The designed metamaterial absorbers are composed of a top 50 nm-thick tungsten (W) layer patterned with cross resonators, a 200 nm-thick alumina ( $\text{Al}_2\text{O}_3$ ) spacer layer and a 200 nm-thick tungsten ground plane on a silicon substrate, denoted as  $t_h$ ,  $t_d$  and  $t_m$ , respectively. The thicknesses of top tungsten layer and spacer layer are selected to optimize the absorption performance and fabrication quality for the following absorber designs. The thick tungsten ground plane will effectively block the transmission so that the absorption is equal to unity minus the reflection. Figure 1(a) presents the schematics of single-sized unit cells of cross resonators A, B, C and D with the same geometrical parameters of period ( $P = 1500$  nm) and arm width ( $w = 450$  nm) but different arm lengths  $L$  of  $0.87P$ ,  $0.77P$ ,  $0.67P$  and  $0.57P$ , respectively. As shown in Figs. 1(b)–1(d), by combining two, three or four cross resonators of

different sizes in one double-sized unit cell, metamaterial absorber patterns of ADAD, ABCC, and ABCD are obtained for realizing flexibly tunable absorption band.

Geometrical parameters of metamaterial absorbers are optimized with numerical simulation (COMSOL Multiphysics), by starting from a single-sized unit cell of cross resonator with  $P = 900$  nm,  $L = 800$  nm and  $w = 300$  nm at normal incidence under averaged TE and TM polarizations. Figures 2(a)–2(c) give the simulated polarization-averaged absorption spectra of single-sized unit cells as functions of period, arm length and arm width, where two main absorption peaks are observed. The absorption peak at around  $1.5 \mu\text{m}$  is due to the grating effect of coupled cross resonators, showing less dependence on the geometrical parameters of cross resonators. Another absorption peak at longer wavelength arises from the magnetic resonance of cross resonator, exhibiting a strong dependence on the period and arm length but not arm width. Moreover, Figs. 2(d)–2(f) show the absorption spectra of three different types of double-sized unit cells with patterns of ADAD, ABCC and ABCD by changing the unit cell period, where dual-band and broadband near-perfect absorption at mid-infrared range are achieved. In experiment, the unit cell period of  $P = 1500$  nm is used by considering a balance between high absorption and relatively wide bandwidth for double-sized unit cells.

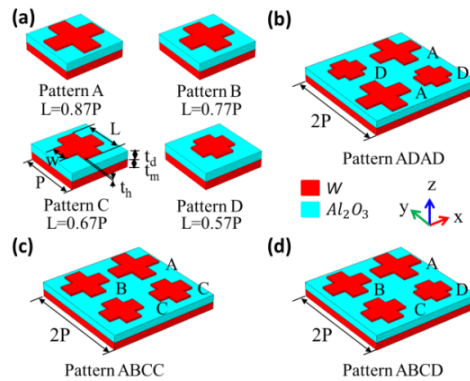


Fig. 1. Schematics of the unit cells of wavelength-selective metamaterial absorbers with tungsten cross resonators. (a) Single-sized unit cells of cross resonators A, B, C and D with the same period  $P$  and arm width  $w$  but different arm length  $L$ . (b - d) The combination of two, three or four cross resonators of different sizes in one double-sized unit cell, forming the patterns of ADAD, ABCC, and ABCD, respectively.

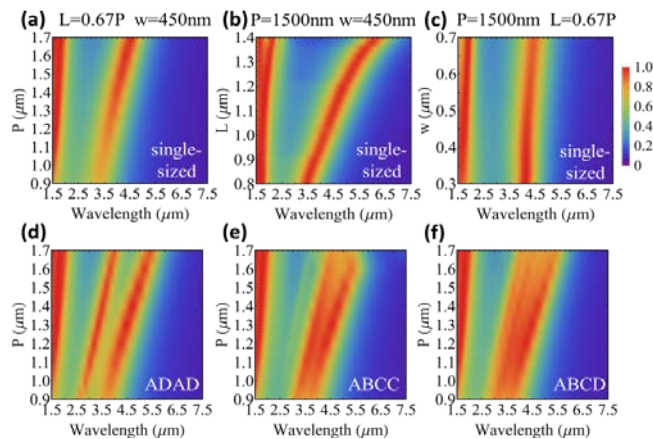


Fig. 2. Simulated polarization-averaged absorption spectra of metamaterial absorbers as functions of geometrical parameters at normal incidence, for single-sized unit cells with varying (a) period  $P$ , (b) arm length  $L$  and (c) arm width  $w$ , and for double-sized unit cells of (d) ADAD, (e) ABCC and (f) ABCD with varying period  $P$ .

The W-Al<sub>2</sub>O<sub>3</sub>-W three-layer stack is grown by RF sputtering on a silicon substrate. The W is grown in Ar atmosphere at 6 mTorr pressure at a deposition rate of 0.75 Å / sec and the Al<sub>2</sub>O<sub>3</sub> is grown in Ar atmosphere at 5 mTorr pressure at a rate of 0.08 Å / sec. The designed cross resonator patterns are fabricated with focused ion beam (FIB) milling on the top tungsten layer. Figures 3(a)–3(d) show scanning electron microscopy (SEM) images of the fabricated metamaterial absorbers with cross resonator array patterns of C, ADAD, ABCC and ABCD, with the geometrical parameters of cross resonators A, B, C and D described in Fig. 1(a). Due to the strong atomic bonding force and high hardness of W, the FIB milled W cross resonators have relatively rough side walls, compared with other metals such as Au [38], Ag [39] and Al [40,41]. Such imperfections in the fabrication process gives an averaged variation of  $\pm 15$  nm in the geometrical parameters of cross resonators different from the design. The absorption spectra of the metamaterial absorbers are obtained from the measured reflection spectra at normal incidence using Fourier transform infrared spectroscopy (FTIR). The measured reflection spectra are normalized with the reflection from a high-quality gold mirror. Numerical simulation is further conducted with the geometrical parameters of cross resonators obtained from the SEM images, where the permittivity of W and Al<sub>2</sub>O<sub>3</sub> is from Rakic [42] and Kischkat [43], respectively.

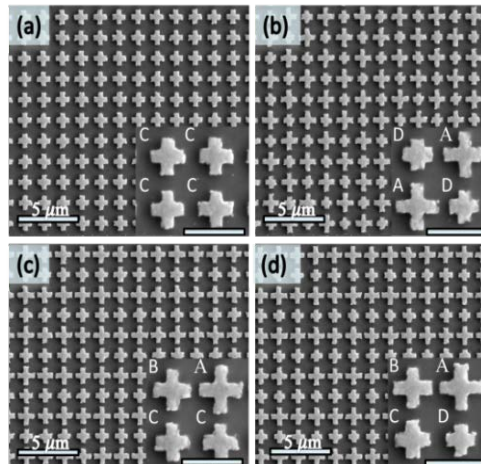


Fig. 3. SEM images of the fabricated metamaterial absorbers, showing the cross resonator arrays for unit cell patterns of (a) C, (b) ADAD, (c) ABCC and (d) ABCD. The scale bar inside the insert image is 1  $\mu\text{m}$ .

Figure 4 shows the experimental unpolarized absorption spectra (solid lines) at normal incidence for different unit cell patterns, where the simulated polarization-averaged absorption spectra (dashed lines) are also plotted for comparison. In Fig. 4(a), it shows the absorption spectra of single-sized unit cell patterns of A, B, C and D with  $P = 1500$  nm and  $w = 450$  nm but  $L = 0.87P, 0.77P, 0.67P$  and  $0.57P$ , respectively. A near perfect absorption peak induced by the magnetic resonance of the cross resonator shows red shift with the increased arm length, allowing the widely tunable absorption band ranging from 3.5  $\mu\text{m}$  to 5.5  $\mu\text{m}$ , which differs from the almost fixed absorption peak at 1.73  $\mu\text{m}$  due to the grating effect of coupled cross resonators. The deviation between the experimental and simulation results can be explained by the imperfect geometries in the fabricated cross resonators and the variation of permittivity. The influence of period is shown in Fig. 4(b) for the double-sized unit cell pattern ADAD. Two individual absorption peaks at longer wavelength arising from resonator A and D in the double-sized unit cell pattern ADAD exhibit red shift with the increased period and the fixed arm width, however, a mitigation of the absorption appears due to the reduced effective light-cross resonator interaction volume. Additionally, the improved

absorption has been observed by increasing the arm width  $w$  from 450 nm to 600 nm. The structure with larger arm width has higher fabrication tolerance, and the effect of roughness on absorption is less compared to the structure with smaller arm width.

More continuous absorption bands are realized with the double-sized unit cell patterns of ABCC and ABCD, as shown in Figs. 4(c) and 4(d), respectively. With  $P = 1500$  nm and  $w = 600$  nm, pattern ABCC shows an absorption band of around 900 nm with the absorption intensity over 0.9 (the maximum of 0.93). And the absorption band is about  $1 \mu\text{m}$  ( $1.2 \mu\text{m}$ ) for the absorption intensity over 0.88 (0.85) for pattern ABCD. Compared with the absorption spectra of pattern ABCC, the single-sized unit cell D slightly broadens the absorption band to the shorter wavelength range in pattern ABCD, but it also affects the absorption intensity due to the weak coupling with neighboring resonators. Furthermore, a near perfect absorption band is observed in experiment for pattern ABCD with  $P = 1100$  nm and  $w = 450$  nm, having the absorption intensity over 0.94 (the maximum of 0.96) from  $3.22 \mu\text{m}$  to  $4 \mu\text{m}$ .

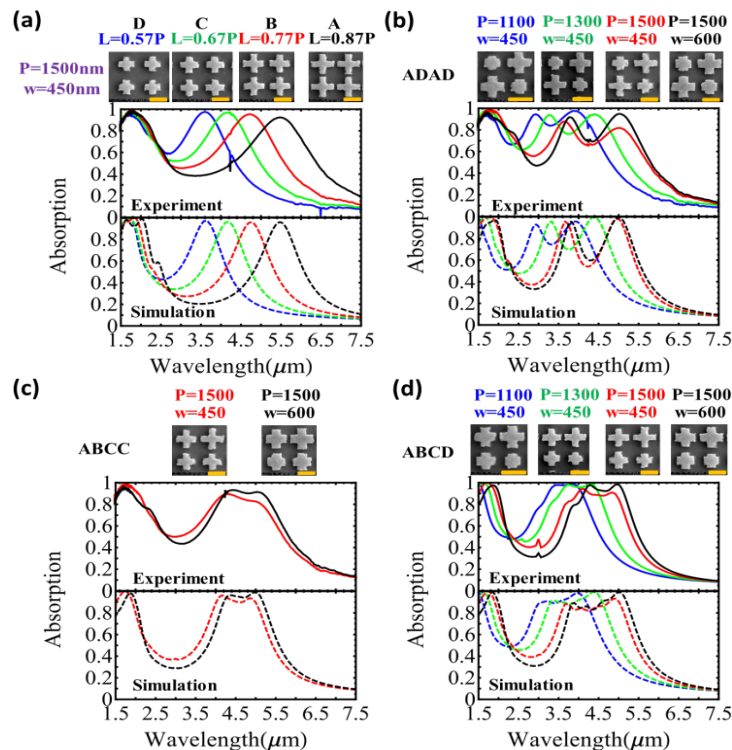


Fig. 4. Experimental (unpolarized) and simulated (polarization-averaged) absorption spectra at normal incidence for cross resonator arrays with different unit cell patterns. (a) A, B, C and D with  $P = 1500$  nm and  $w = 450$  nm but  $L = 0.87P$ ,  $0.77P$ ,  $0.67P$  and  $0.57P$ , respectively. (b) ADAD with  $P = 1100$  nm,  $1300$  nm and  $1500$  nm. (c) ABCC with different  $w$  but same  $P$  and  $L$ . (d) ABCD with different  $P$ . The scale bar of the SEM image is  $1 \mu\text{m}$ .

### 3. Optical mode analysis and equivalent circuit model

In Fig. 5, cross sections of magnetic field  $H_y$  distributions along the  $x$ - $z$  plane across the unit cells are plotted under TM polarization (electric field is along  $x$  direction) at normal incidence, where the location of each cross section view is illustrated in Figs. 5(e1)-5(e4). Figures 5(a1)-5(a3) show the magnetic field distributions in unit cell pattern C at the wavelength of  $4.17 \mu\text{m}$  and  $1.73 \mu\text{m}$ , representing the first-order and high-order magnetic resonance modes along the horizontal cross arm along the  $x$  direction, respectively. The black arrows represent the direction and magnitude of the induced electric current density. The magnetic resonance arises from the antiparallel currents of electric charges in the W layers

excited by the incident light [2]. There is one induced current loop between the top W resonator and the ground plane for the first-order magnetic resonance at  $4.17 \mu\text{m}$  in Fig. 5(a1). For the high-order magnetic resonance at  $1.73 \mu\text{m}$  in Fig. 5(a2), there are multiple induced current loops observed with the coupling between neighboring cross resonators. This type of resonance at short wavelength is related to the grating effect of coupled cross resonators, and the cross-talk effect between the neighboring cross resonators manifests itself by the connected induced current loops. Moreover, as shown in Figs. 5(b)-5(d), the first-order magnetic resonance and induced current loop are also found in the magnetic field distributions at longer wavelengths for double-sized unit cell patterns. The combination of the multiple first-order magnetic resonances in cross resonators with different sizes are responsible for the generation of absorption bands with different bandwidth and absorption intensity [25–27].

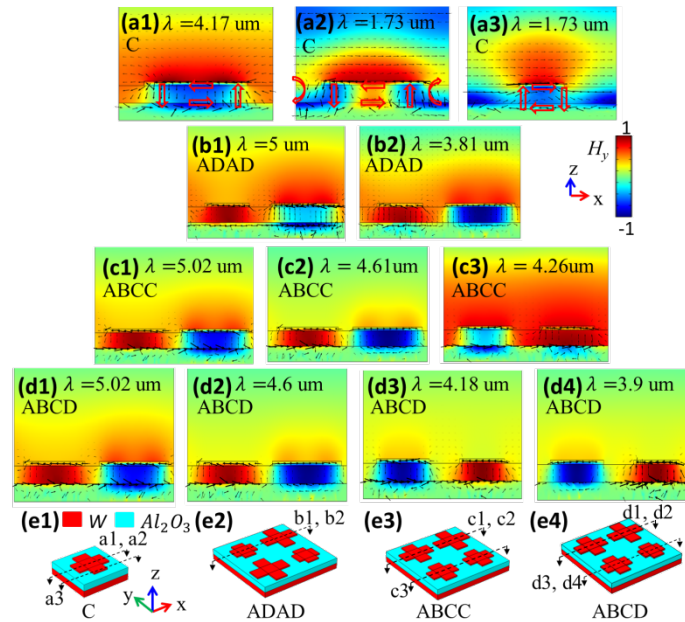


Fig. 5. Cross section view of the normalized magnetic field  $H_y$  distribution at different resonance wavelengths under TM polarization at normal incidence for the designed unit cell patterns of (a1 - a3) C, (b1 - b2) ADAD, (c1 - c3) ABCC and (c1 - c4) ABCD. The black arrows represent the induced current density. (e1 - e4) Schematics of the locations of cross sections in the designed unit cells.

In order to develop further understanding of absorption performance, the dispersion relations of designed metamaterial absorbers are plotted through the simulated absorption spectra as a function of wave number  $\lambda^{-1}$  and in-plane wave vector  $k_x$  normalized with half of the reciprocal lattice vector  $k_d = \pi/P$ . The results are shown in Fig. 6 for unit cell patterns of A, D, and ABCD under TM and TE polarization, respectively. It shows that there is almost no dependence of the absorption peak and band on the incident angle for the first-order magnetic resonances at long wavelengths larger than  $2.5 \mu\text{m}$  (below  $4000 \text{ cm}^{-1}$ ), which is a significant advantage for absorber or emitter applications with omnidirectional requirements. However, for the high-order magnetic resonance at high wave number larger than  $4000 \text{ cm}^{-1}$ , the absorption branch is strongly modified by the grating effect of coupled cross resonators, with the excitation of spoof surface plasmons [16,25,44,45]. The dispersion relation of surface plasmons is described as  $|\mathbf{k}_{\text{spp}}| = (\omega/c) \sqrt{\varepsilon_1 \varepsilon_2 / (\varepsilon_1 + \varepsilon_2)}$ , where  $\varepsilon_1$  and  $\varepsilon_2$  denotes the permittivity of metal and dielectric, respectively. It is noted that spoof surface plasmons are

usually considered for 1D or 2D periodic metamaterials under TM polarization [44,46], however, spoof surface plasmons also exist under TE polarization for 2D case [45]. For a 2D periodic metamaterial absorber, to excite spoof surface plasmons, momentum matching condition (i.e.  $\mathbf{k}_{\text{spp}} = \mathbf{k}_{\parallel, \text{inc}} + \mathbf{k}_{\text{g}}$ ) must be achieved at a specific wavelength.  $\mathbf{k}_{\parallel, \text{inc}} = k_{x, \text{inc}} \mathbf{x} + k_{y, \text{inc}} \mathbf{y}$  representing the wave vector of the tangential component of the incident light in the x-y plane.  $\mathbf{k}_{\text{g}}$  is the reciprocal lattice vector of the Bloch wave for the grating with  $\mathbf{k}_{\text{g}} = 2\pi m/P \mathbf{x} + 2\pi n/P \mathbf{y}$ , where m and n are the grating diffraction order along the x and y direction, respectively. The wave vector of spoof surface plasmons is then a function of unit cell period and incident angle, which is observed in Fig. 6. The excitation of different diffraction orders of spoof surface plasmons depends on the incident polarization. For TM polarized incidence with only  $k_{x, \text{inc}}$ ,  $|\mathbf{k}_{\text{spp}}| = |k_{x, \text{inc}} + |2\pi m/P|$  with  $k_{x, \text{inc}} = (\omega/c)\sin\theta$  and the assumption of  $n = 0$ . The branches with diffraction orders of  $m = \pm 1$  are plotted with white dashed lines in Figs. 6(a1)–(c1) from the theoretical dispersion relation. In addition, the diffraction orders with  $m = 0$  and  $n = \pm 1$  are shown under TM polarization following the relation of  $|\mathbf{k}_{\text{spp}}| = \sqrt{(\omega \sin\theta / c)^2 + (2\pi n/P)^2}$ , which are attributed to the electric field component along the y direction of the diffracted wave. Furthermore, in Figs. 6(a2)–6(c2), the diffraction orders with  $m = 0$  and  $n = \pm 1$  are plotted under TE polarization where the above dispersion relation is still followed, where the incident electric field is dominant along y direction with  $k_{x, \text{inc}} = 0$ . The dispersion curve shows blue shift with the increased incidence angle for the TE case. The above dispersion analysis explains the strong interactions between the high-order magnetic resonances of neighboring cross resonators and the excitation of spoof surface plasmons at short wavelength range [45,47].

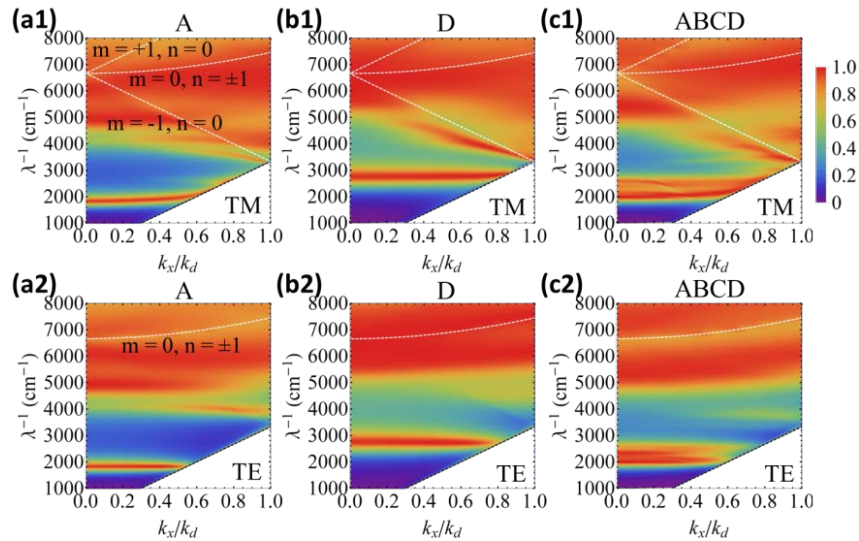


Fig. 6. Dispersion relation of unit cell patterns of A, D, and ABCD under (a1 - c1) TM and (a2 - c2) TE polarization, respectively. The white dashed lines are obtained from the grating dispersion relations at different diffraction orders.

In order to obtain an intuitive description of the underlying mechanism for magnetic resonance characteristics, the designed cross resonators are analyzed with the equivalent RLC circuit model [48,49] to model not only the first-order magnetic resonance and its coupling but also the impedance of the effective multilayer stack. Figure 7(a) shows the equivalent RLC circuit model of the single-sized unit cell pattern C. The total impedance  $Z_C$  is composed

of the impedance from unit cell pattern  $Z_{C0}$  and the impedance of the effective multilayer stack  $Z_{ms}$ . For  $Z_{C0}$ , two types of capacitance are considered, the parallel capacitance between the top  $W$  resonator and ground plane  $C_d = \phi_1 \epsilon_0 \epsilon_d (2Lw - w^2)/t_d$  and an approximated gap capacitance between neighboring resonators  $C_g = \phi_2 \epsilon_0 \epsilon_d w t_h / (P - L)$ , where  $\epsilon_0$  is the permittivity in the free space,  $\phi_1$  and  $\phi_2$  are numerical factors to approximate the non-uniform distribution of charges due to the induced electric currents [48,49]. Furthermore,  $L_m$  is employed to represent the mutual magnetic inductance from stored magnetic energy between the top  $W$  resonator and the ground plane, while  $L_k$  accounts for the kinetic inductance induced from the kinetic movement of free charge carriers inside the  $W$  layers.  $L_m = \phi_3 \mu_0 L t_d / w$  with the permeability of free space,  $\mu_0$ , and the numerical factor,  $\phi_3$ , to rectify the geometrical approximation.  $L_k$  can be derived from the complex kinetic impedance  $Z_k = R_k - i\omega L_k$  with  $Z_k = L / (A_{eff} \tilde{\sigma})$  and  $A_{eff} = \phi_4 w \lambda / (2\pi\kappa)$ .  $A_{eff}$  denotes the effective area across

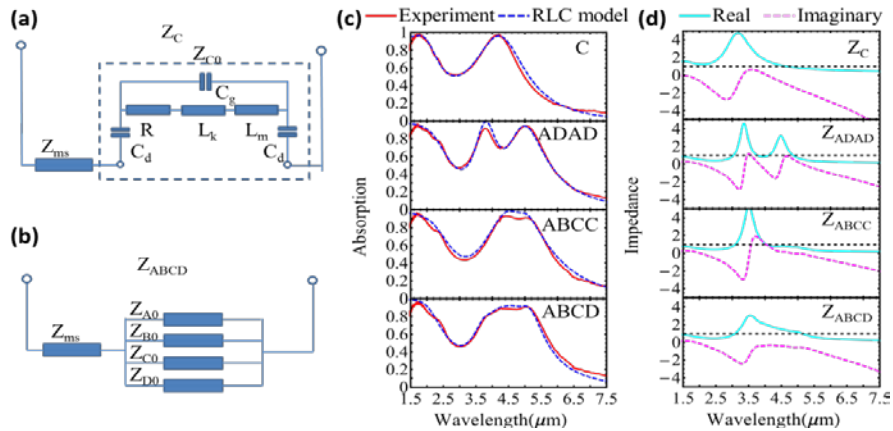


Fig. 7. Equivalent RLC circuit model of the designed unit cells of cross resonators. (a) Single-sized unit cell of C. (b) Double-sized unit cell pattern of ABCD. (c) Unpolarized absorption spectra obtained from experiment and equivalent RLC model at normal incidence for unit cell patterns of C, ADAD, ABCD and ABCD. (d) The real and imaginary parts of normalized impedance calculated from equivalent RLC model. The dashed line is at the impedance of 1.

the induced current path obtained from the multiplication of arm width and skin depth of  $W$ , with the extinction coefficient [50] and the numerical factor  $\phi_4$ . The complex conductivity of  $W$  reads  $\tilde{\sigma} = \sigma' + i\sigma''$ , where  $\sigma' = \omega\epsilon_0\epsilon_m''$  and  $\sigma'' = -\omega\epsilon_0\epsilon_m'$  are derived from Maxwell's equations by considering the conduction current density and displacement current density [50]. Therefore,  $R_k$  and  $L_k$  can be solved from the real part and imaginary part of  $Z_k$ , respectively. Additionally, the impedance of the effective multilayer stack  $Z_{ms}$  can be calculated from the impedance transformation method [51]. This method is based on the recursion relation of  $Z_j = \eta_j (Z_{j+1} + i\eta_j \tan k_j d_j) / (\eta_j + iZ_{j+1} \tan k_j d_j)$ ,  $j = 2, 1$ , with the initialization of  $Z_3 = \eta_3$ , where  $\eta_j = \sqrt{\mu_0 / (\epsilon_0 \epsilon_j)}$  expresses the intrinsic impedance of the  $j$ th layer with thickness  $d_j$  and refractive index  $n_j$ . The impedance of vacuum is  $Z_0 = \sqrt{\mu_0 / \epsilon_0}$ .  $k_j$  is the wave vector at the  $j$ th layer with  $k_j = n_j k_0$ , where  $k_0$  denotes the wave vector in free space. The impedance of the effective multilayer stack is then obtained by the relation  $Z_{ms} = \phi_5 Z_1$ , where  $\phi_5$  is numerical factor to account for the influence from the cross resonator pattern in the effective multilayer stack assumption. Finally, the total impedance of single-sized unit cell pattern C is obtained by  $Z_c = Z_{ms} + (Z_k + i\omega L_m) / [1 + i\omega C_g (Z_k + i\omega L_m)] + 2$

/ ( $i\omega C_d$ ). As shown in Fig. 7(b), regarding the impedance of multiple cross resonators, a parallel circuit connecting each single-sized unit cell is employed to evaluate the coupling effect of multiple resonances for the double-sized unit cell patterns of ABCD, with the impedance of each cross resonator denoted as  $Z_{A0}$ ,  $Z_{B0}$ ,  $Z_{C0}$  and  $Z_{D0}$ , respectively. To simplify the problem, a homogenization assumption is used by setting the same value for each type of numerical factor ( $\phi_1, \phi_2, \phi_3, \phi_4$ ), and the same value for gap capacitance between neighboring resonators with  $C_g = \phi_2 \varepsilon_0 \varepsilon_d w_h/d_{\text{eff}}$ , where the effective distance  $d_{\text{eff}} = [(2P - L_A - L_B) + (2P - L_B - L_C) + (2P - L_C - L_D) + (2P - L_A - L_D)]/4$ . The total impedance of the whole unit cell pattern of ABCD reads  $Z_{\text{ABCD}} = Z_{\text{ms}} + (1/Z_{A0} + 1/Z_{B0} + 1/Z_{C0} + 1/Z_{D0})$ . The absorption spectrum is consequently calculated by  $A = 1 - [(Z_{\text{ABCD}} - Z_0) / (Z_{\text{ABCD}} + Z_0)]^2$ . Figure 7(c) plots the equivalent RLC model calculated unpolarized absorption spectra for metamaterial absorbers with unit cell patterns of C, ADAD, ABCC and ABCD, respectively, showing a good agreement with the measured results. Accordingly, Fig. 7(d) shows the real and imaginary parts of the total effective impedance  $Z_{\text{total}}$  of the designed metamaterial absorbers, normalized by the  $Z_0$  of free space. The absorption performance can be alternatively explained through the impedance match theory [4]. When  $Z_{\text{total}}/Z_0$  approaches 1, there is no reflected wave and a strong absorption band will appear in the absorption spectrum.

#### 4. Thermal analysis for absorbers and energy conversion efficiency for emitters

As the incident light wave is coupled into the metamaterial absorber, heat is generated due to the optical loss of the W layers and the time-averaged dissipative energy density per unit volume is written as  $Q_h = \varepsilon_0 \omega \varepsilon_m''(\omega) |E|^2 / 2$ , where  $E$  is the electric field and  $\varepsilon_m''$  is the imaginary part of the metal [52,53]. Figure 8 shows the distributions of the time-averaged dissipative energy density at the cross section of the top W layer for the designed metamaterial absorbers at different resonance wavelengths, with green arrows describing the direction and magnitude of the Poynting vector. The power dissipation density distributions in Fig. 8 are obtained with TM polarized normally incident light with the power of  $22.2 \mu\text{W}/\mu\text{m}^2$  for each type of metamaterial absorber. From the top view of the unit cell pattern of C at two resonance wavelengths in Figs. 8(a1) and 8(a3), the optical energy flow inside the W cross resonators at certain resonant wavelengths generate heat. The cross sections in Figs. 8(a2) and 8(a4) show the optical energy penetration inside the absorbers and both the W resonator and ground plane contribute to the heat generation through dissipative loss. Similar dissipation process happens for metamaterial absorbers with double-sized unit cell patterns of ADAD, ABCC and ABCD, as seen in Figs. 8(b1)-8(b2), 8(c1)-8(c3) and 8(d1)-8(d4), where the specific energy dissipation distribution inside each type of unit cell at certain resonance wavelength is observed.

The generated heat  $Q_d$  serves as the heat source in the transient heat transfer equation  $C_p \rho \partial T / \partial t + \nabla \cdot (-k_c \nabla T) = Q_d$ , where  $C_p$ ,  $\rho$ ,  $k_c$ , are the material dependent specific heat capacity, density and thermal conductivity, respectively. To simplify the heat transfer analysis, the steady-state heat transfer is considered by setting the time derivative component as zero. This equation has been proved valid for a nanoscale material system, however, the parameter of thermal conductivity needs to be modified accordingly for thin films [53–56]. It has been theoretically and experimentally pointed out that the thermal conductivity of a thin film at the nanoscale dramatically decreases since the interfacial scattering effects between similar or dissimilar materials inside the structure significantly impede the vibrational energy transfer across the interfaces [55]. To simplify the problem, specific heat capacity and density can still be the same as bulk material. Thermal parameters used in this work are listed in Table 1 [53–56]. To solve the heat transfer problem, proper boundary conditions are imposed on the designed metamaterial absorber. At the bottom of the  $100 \mu\text{m}$ -thick silicon substrate, a Dirichlet boundary condition is used by setting a constant temperature  $T = T_0$ , where  $T_0$  is the

room temperature of 300 K. Following the boundary conditions used in [53], the heat generation and temperature distribution is solved for metamaterial absorbers using COMSOL Multiphysics.

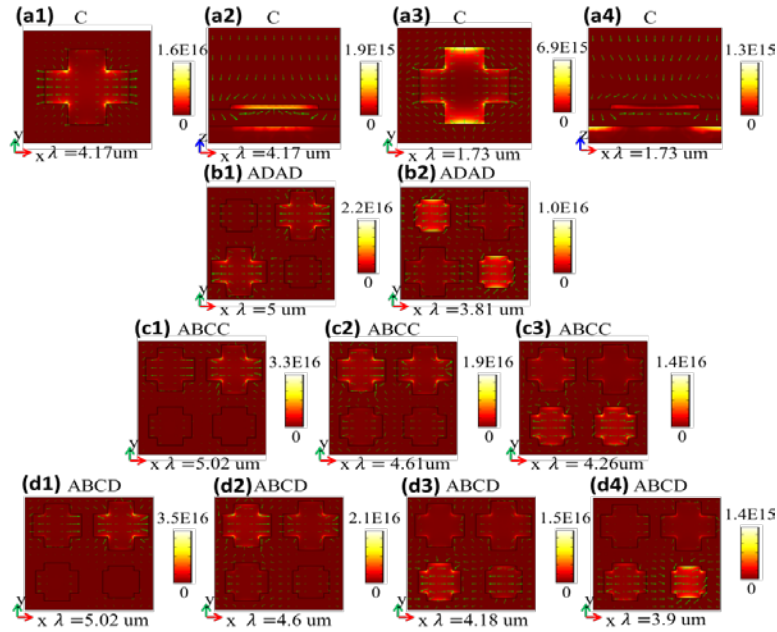


Fig. 8. Time-averaged optical power dissipation density  $Q_h$  (W/m<sup>3</sup>) distributions at the cross section (x-y plane) of top W layer for unit cell patterns of (a1, a3) C, (b1, b2) ADAD, (c1 - c3) ABCC and (d1 - d4) ABCD at different resonance wavelengths under normal incidence. Cross section (x-z plane) of single-sized unit cell pattern of C is shown in (a2) and (a4). Green arrows show the direction and magnitude of Poynting vector.

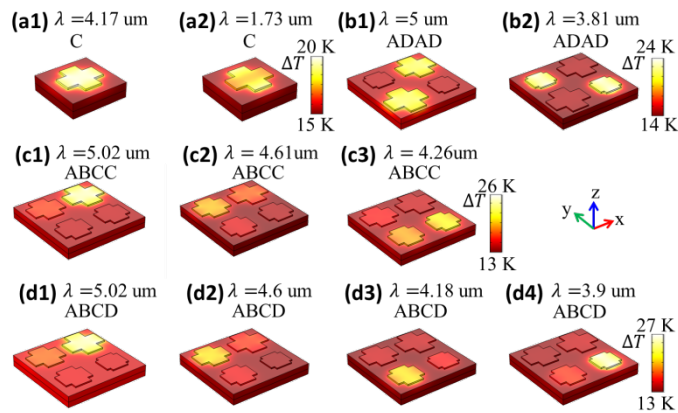


Fig. 9. Temperature distributions for unit cell patterns of (a1, a2) C, (b1, b2) ADAD, (c1 - c3) ABCC and (d1 - d4) ABCD at different resonance wavelengths under TM polarized normal incidence. It is noted that the incident optical power density is 22.2  $\mu\text{W}/\mu\text{m}^2$  and the 100  $\mu\text{m}$ -thick silicon substrate is not shown.

Figure 9 shows the calculated steady-state temperature distributions in cross resonators generated by heat source from the dissipative energy for metamaterial absorbers with unit cell patterns of C, ADAD, ABCC and ABCD at different resonance wavelengths. It is noted that the 100  $\mu\text{m}$ -thick silicon substrate is not shown in the plot. For a single-sized unit cell pattern of C shown in Figs. 9(a1)-9(a2), a temperature variation range from 315 K to 320 K is found

at  $\lambda = 4.17 \mu\text{m}$  and the highest temperature appears in the horizontal arm of the W cross resonator. A similar temperature range is found at  $\lambda = 1.73 \mu\text{m}$  but with the highest temperature in the vertical arm of the W cross resonator. The magnitude of temperature distribution is consistent with the time-averaged dissipative energy density  $Q_h$  serving as the heat source. For the double-sized unit cell patterns of ADAD, ABCC and ABCD, high temperature regions are distributed in the specific W cross resonators at certain resonance wavelengths. When comparing the temperature distribution of single-sized unit cell patterns of C at  $\lambda = 4.17 \mu\text{m}$  (with maximum T of 313 K and minimum T of 308 K) with double-sized unit cell pattern of ABCD at  $\lambda = 4.18 \mu\text{m}$  (with maximum T of 314 K and minimum T of 306 K), one can find a relatively higher maximum temperature but a lower minimum temperature for the double-sized unit cell pattern, which is due to the coupling effects between neighboring cross resonators and hence a different heat dissipation environment for each type of unit cell pattern.

**Table 1. Physical properties of materials for heat transfer analysis**

	$\rho$ (kg m <sup>-3</sup> )	$C_p$ (J kg <sup>-1</sup> K <sup>-1</sup> )	$k_c$ (W m <sup>-1</sup> K <sup>-1</sup> )
Tungsten	19300	132	52.2 (thickness, 200 nm) 17.4 (thickness, 50 nm)
Alumina	3970	765	1.6
Silicon	2330	712	148
Air	1	353 [K] / T	0.03

The designed W-based metamaterial absorbers and emitters can advance promising applications in thermal energy harvesting such as thermal photovoltaic (TPV) cells at the mid-infrared wavelength range. Different from conventional solar cells, many types of heat sources are available for TPV cells such as high-temperature combustion processes (typically above 2000 K) and low-temperature waste heat sources (typically in 600 K ~1300 K) from industries of glass, steel and paper [57,58]. High-temperature TPV cells are still difficult to implement in practice mainly due to the requirement of high-temperature enduring materials and thermal management [57]. Low-temperature TPV cells are important for energy recovery from waste heat sources and have been experimentally explored with low-bandgap semiconductor of InAs (0.32 eV) [58]. Alternative selections of low-bandgap semiconductors (0.18 eV – 0.35 eV), for instance, InSb (0.18 eV) [59], SnTe (0.18 eV) [60], PbTe (0.19 eV) [61], PbSe (0.26 eV ~0.29 eV) [62,63], InAsSb (0.29 eV) [64] and GaInAsSbP (0.35 eV) [65], have also been reported for designing practical low-temperature TPV cells.

The common configuration of the TPV cell has been schematically shown in the literature [8,13]. The energy conversion efficiency of TPV cells is mainly determined by both the thermal emission spectrum of the emitter and the semiconductor selection as pointed out from the detailed balance efficiency [8,10,66]. To simplify the problem, the photon recycling process of sub-bandgap photons or re-emitted photons can be ignored, which is considered as an improvement of the overall conversion efficiency [8]. It assumes that the quantum efficiency of the semiconductor exactly cuts off at the bandgap energy ( $E_g$ ). Each photon with energy ( $\zeta$ ) greater than the bandgap energy can excite an electron-hole carrier pair with energy of  $E_g$ . The overall conversion efficiency of TPV cell  $\eta$  is evaluated as the fraction of converted electrical power to input power from thermal emitter, described by  $\eta = U(T, E_g) \nu(T, E_g) M(V_{op})$  [8], where  $U$  is the ultimate conversion efficiency which imposes a cutoff on the irradiance power allowing to be converted from thermal emitter,  $\nu$  takes account into the recombination process, and  $M$  presents the consideration on

maximizing the overall conversion efficiency of the TPV cell by optimizing the selection of open-circuit voltage ( $V_{op}$ ). As defined in [8],

$$U(T, E_g) = \frac{\int_0^{\pi/2} d\theta \sin(2\theta) \int_{E_g}^{\infty} d\zeta E_m(\zeta, \theta) I_{BB}(\zeta, T_e) E_g / \zeta}{\int_0^{\pi/2} d\theta \sin(2\theta) \int_0^{\infty} d\zeta E_m(\zeta, \theta) I_{BB}(\zeta, T_e)} \quad (1)$$

where  $E_m(\zeta, \theta) = (\langle A_{TE}(\zeta, \theta) \rangle + \langle A_{TE}(\zeta, \theta) \rangle) / 2$  is the emissivity obtained from polarization and incident angle averaged absorption spectra according to the Kirchhoff's law,

$I_{BB} = 2\zeta^3 / [h^3 c^2 (\text{Exp}(\frac{\zeta}{k_B T}) - 1)]$  is the spectral radiance of an ideal blackbody. It finds that

the ultimate efficiency is highly dependent on the operating temperature and bandgap energy, which is essentially related with the power that can be used for electric generation. Optimum useful power is obtained when emissivity of designed selective emitter is matched to that of a blackbody. However, taking account into the recombination process and actual difference between open-circuit voltage  $V_{op}$  and bandgap voltage  $V_g$ , ultimate efficiency is reduced by the second term, expressed as [8]

$$\nu(T, E_g) = V_{op} / V_g = V_c / V_g \ln \left[ f Q_e(T, E_g) / Q_c(T_c, E_g) \right] \quad (2)$$

Bandgap voltage is written as  $V_g = E_g / e$ , where  $e$  is an electron's charge; initial cell voltage at cell temperature  $T_c$  is written as  $V_c = E_g / e$ . The non-ideality factor  $f$  is usually set as 0.5 to consider the influence from non-radiative recombination and non-unity absorption in the TPV cell [8]. For the TPV cell, the fraction of incident photon number flux resulting from the designed emitter and an ideal blackbody at temperature of  $T_c$  reads [8]

$$Q_e / Q_c = \left[ \int_0^{\pi/2} d\theta \sin(2\theta) \int_{E_g}^{\infty} d\zeta \pi E_m(\zeta, \theta) I_{BB}(\zeta, T_e) / \zeta \right] / \left[ \int_{E_g}^{\infty} d\zeta \pi I_{BB}(\zeta, T_c) / \zeta \right] \quad (3)$$

The last consideration is on impedance matching term  $M$ , aiming at maximizing the conversion efficiency by optimizing the selection of open-circuit voltage. The expression is given by [8]

$$M = z_m^2 / \left[ (1 + z_m - e^{-z_m})(z_m + \ln(1 + z_m)) \right] \quad (4)$$

where  $z_m$  is solved from the relation  $z_m + \ln(1 + z_m) = V_{op} / V_c$ .

Figure 10 plots the distributions of ultimate efficiency  $U$  and overall conversion efficiency  $\eta$  as functions of the thermal emitter temperature and semiconductor bandgap energy. Compared to the unit cell pattern of D in Fig. 10(b1), the high  $U$  region (over 0.5) for the unit cell pattern A in Fig. 10(a1) is shifted to the area with lower bandgap energy and lower operating temperature. This is mainly because the energy matching condition between the wavelength-selective emissivity spectrum of the thermal emitter and the temperature dependent blackbody radiation spectrum [8]. The center emission wavelength for the emitter with unit cell pattern of A is around  $5.5 \mu\text{m}$  (0.225 eV), which corresponds to the blackbody temperature of 530 K, giving the maximum  $U$  over 0.5 at temperature below 1000 K (even as low as 500 K) and semiconductor bandgap energy below 0.21 eV. While the emitter with unit cell pattern of D has the center emission wavelength around  $3.5 \mu\text{m}$  (0.354 eV) corresponding to the blackbody temperature of 830 K, the maximum  $U$  over 0.5 is located at temperature above 1150 K and semiconductor bandgap energy above 0.24 eV. Due to the fact

that resonance wavelength of the emitter is located in the mid-infrared range,  $U$  is lower than the reported design in the near-infrared range [8], but the current thermal emitter design exhibits the advantage of operating at low temperature. For instance, an overall conversion efficiency  $\eta$  of 0.1 at temperature 685 K or  $\eta$  of 0.2 at temperature 1080 K can be enabled by using InSb (0.18 eV) with the unit cell pattern of A in Fig. 10(a2). Also, the similar  $\eta$  value can be achieved by using InAsSb (0.29 eV) with the unit cell pattern of D in Fig. 10(b2) at a relatively higher temperature. For the unit cell pattern of D, at the working temperature of 1800 K,  $\eta$  of 0.31 is obtained which is the same as the Shockley-Queisser limit of traditional solar cells. In Fig. 10(c1), the emitter with double-sized unit cell pattern of ABCD shows a region with  $U$  over 0.5 at lower bandgap energy because of the dominant contribution from the unit cell pattern of A with the resonance wavelength around 5.5  $\mu\text{m}$ . Also, one can find in Fig. 10(c2) that the double-sized unit cell enables the TPV cells to operate at low emitter temperature with low semiconductor bandgap energy at the same time for achieving the same overall conversion efficiency. Therefore, the current mid-infrared metamaterial emitters based on multiple W cross resonators are promising in low-temperature waste heat recycling for low power electronic products.

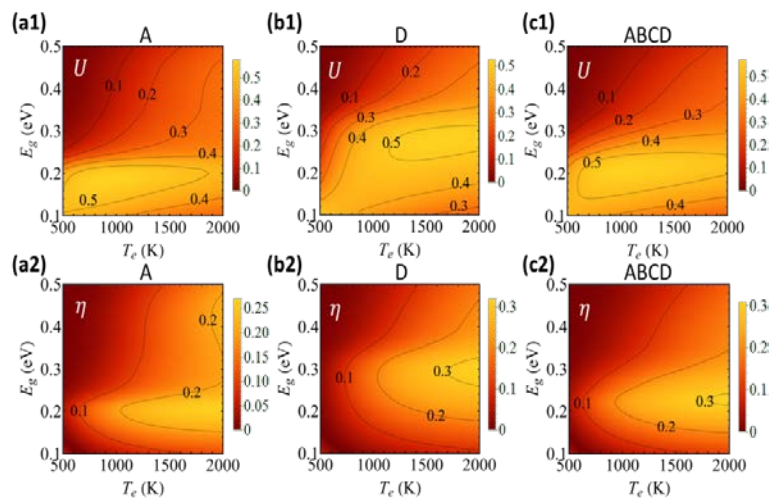


Fig. 10. Ultimate conversion efficiency ( $U$ ) as the function of thermal emitter temperature and the semiconductor band gap energy for unit cell patterns of (a1) A, (b1) D and (c1) ABCD. Overall conversion efficiency ( $\eta$ ) of the TPV system for unit cell patterns of (a2) A, (b2) D and (c2) ABCD.

## 5. Conclusion

In summary, single-sized and double-sized unit cells patterns with tungsten cross resonators have been demonstrated to realize wavelength-selective metamaterial absorbers and emitters in the mid-infrared range, with near-perfect single absorption peaks tunable from 3.5  $\mu\text{m}$  to 5.5  $\mu\text{m}$  and broadband absorption with bandwidth of about 1  $\mu\text{m}$  within the wavelength range from 3  $\mu\text{m}$  to 5.2  $\mu\text{m}$ . The obtained absorption peak is mainly explained by the magnetic resonance supported in the cross resonator unit cells and the dispersion relation of unit cell array under both TM and TE polarizations. An equivalent RLC circuit model is developed to study the characteristics of absorption and impedance spectra for different unit cell patterns based on the magnetic resonance. Furthermore, heat generation and dissipation is analyzed for absorber applications. Thermal energy conversion efficiency is also calculated for realizing feasible TPV systems based on mid-infrared thermal emitter operating at low temperature with low-bandgap semiconductors for applications of low power electronics.

**Funding**

National Science Foundation (NSF) (ECCS-1653032, DMR-1552871); Office of Naval Research (ONR) (N00014-16-1-2408); U.S. Department of Energy, Office of Science, under Contract No. DE-AC02-06CH11357).

**Acknowledgments**

The authors acknowledge the facility support from the Materials Research Center at Missouri S&T. This work was performed, in part, at the Center for Nanoscale Materials, a U.S. Department of Energy Office of Science User Facility, and supported by the U.S. Department of Energy, Office of Science, under Contract No. DE-AC02-06CH11357.